



UNIVERSITY OF LEEDS

This is a repository copy of *Investigating the generalisation of an atlas-based synthetic-CT algorithm to another centre and MR scanner for prostate MR-only radiotherapy*.

White Rose Research Online URL for this paper:
<http://eprints.whiterose.ac.uk/124569/>

Version: Accepted Version

Article:

Wyatt, JJ, Dowling, JA, Kelly, CG et al. (6 more authors) (2017) Investigating the generalisation of an atlas-based synthetic-CT algorithm to another centre and MR scanner for prostate MR-only radiotherapy. *Physics in Medicine and Biology*, 62 (24). N548-N560. ISSN 0031-9155

<https://doi.org/10.1088/1361-6560/aa9676>

(c) 2017, Institute of Physics and Engineering in Medicine. This is an author-created, un-copyedited version of an article published *Physics in Medicine and Biology*. IOP Publishing Ltd is not responsible for any errors or omissions in this version of the manuscript or any version derived from it. The Version of Record is available online at: <https://doi.org/10.1088/1361-6560/aa9676>

Reuse

Items deposited in White Rose Research Online are protected by copyright, with all rights reserved unless indicated otherwise. They may be downloaded and/or printed for private study, or other acts as permitted by national copyright laws. The publisher or other rights holders may allow further reproduction and re-use of the full text version. This is indicated by the licence information on the White Rose Research Online record for the item.

Takedown

If you consider content in White Rose Research Online to be in breach of UK law, please notify us by emailing eprints@whiterose.ac.uk including the URL of the record and the reason for the withdrawal request.



eprints@whiterose.ac.uk
<https://eprints.whiterose.ac.uk/>

Investigating the generalisation of an atlas-based synthetic-CT algorithm to another centre and MR scanner for prostate MR-only radiotherapy

Jonathan J. Wyatt¹, Jason A. Dowling², Charles G. Kelly¹, Jill McKenna¹, Emily Johnstone³, Richard Speight⁴, Ann Henry^{3,4}, Peter B. Greer⁵, Hazel M. McCallum¹

¹ Northern Centre for Cancer Care, Newcastle upon Tyne Hospitals, UK

² CSIRO Australian e-Health Research Centre, Australia

³ Leeds Institute of Cancer and Pathology, University of Leeds, UK

⁴ Leeds Cancer Centre, Leeds Teaching Hospitals, UK

⁵ Calvary Mater Newcastle Hospital, Australia

E-mail: jonathanwyatt@nhs.net

Abstract.

There is increasing interest in MR-only radiotherapy planning since it provides superb soft-tissue contrast without the registration uncertainties inherent in a CT-MR registration. However MR images cannot readily provide the electron density information necessary for radiotherapy dose calculation. An algorithm which generates synthetic CT's for dose calculations from MR images of the prostate using an atlas of 3 T MR images has been previously reported by two of the authors. This paper aimed to evaluate this algorithm using MR data acquired at a different field strength and a different centre to the algorithm atlas. 21 prostate patients received planning 1.5 T MR and CT scans with routine immobilisation devices on a flat-top couch set-up using external lasers. The MR receive coils were supported by a coil bridge. Synthetic CT's were generated from the planning MR images with (sCT_{1V}) and without (sCT) a one voxel body contour expansion included in the algorithm. This was to test whether this expansion was required for 1.5 T images. Both synthetic CT's were rigidly registered to the planning CT (pCT). A 6 MV Volumetric Modulated Arc Therapy plan was created on the pCT and recalculated on the sCT and sCT_{1V}. The synthetic CT's dose distributions were compared to the dose distribution calculated on the pCT.

The percentage dose difference at isocentre without the body contour expansion (sCT - pCT) was $\Delta D_{sCT} = (0.9 \pm 0.8)\%$ and with (sCT_{1V} - pCT) was $\Delta D_{sCT_{1V}} = (-0.7 \pm 0.7)\%$ (mean \pm one standard deviation). The sCT_{1V} result was within one standard deviation of zero and agreed with the result reported previously using 3 T MR data. The sCT dose difference only agreed within two standard deviations. The mean \pm one standard deviation gamma pass rate was $\Gamma_{sCT} = 96.1 \pm 2.9\%$ for the sCT and $\Gamma_{sCT_{1V}} = 98.8 \pm 0.5\%$ for the sCT_{1V} (with 2% global dose difference and 2 mm distance to agreement gamma criteria). The one voxel body contour expansion improves the synthetic CT accuracy for MR images acquired at 1.5 T but requires the MR voxel size to be similar to the atlas MR voxel size. This study suggests that the atlas-based algorithm can be generalised to MR data acquired using a different field strength at a different centre.

Keywords: MR-only planning, MRI, radiotherapy, synthetic CT, prostate

Submitted to: *Phys. Med. Biol.*

1. Introduction

The use of Magnetic Resonance (MR) images to delineate the prostate for radiotherapy treatment planning has expanded significantly due to the superb soft-tissue contrast of MR (Khoo & Joon 2006). This has resulted in reduced intra- and inter-observer variability of prostate contours compared to CT (Dubois et al. 1998) and a reduced overall prostate volume (Dubois et al. 1998, Rasch et al. 1999). Typically MR images are registered with a planning Computed Tomography (CT), with the MR used for contour delineation and the CT for radiotherapy planning and dose calculations. This is because the MR signal intensity depends on proton spins, which means that both air and bone will have near zero signal intensities despite having very different electron densities. Therefore MR images cannot be directly calibrated to relate to electron density for radiotherapy dose calculations. Unfortunately the MR-CT registration in prostate radiotherapy treatments can be sub-optimal due to differences in bladder and rectum filling between the two imaging sessions, despite using a bladder and bowel preparation protocol. This results in a significant delineation uncertainty arising from the registration (Nyholm et al. 2009). This uncertainty can be removed by utilising a MR-only planning approach which eliminates the need for a planning CT.

MR-only planning requires a method of providing an electron density map for radiotherapy dose calculations. The most common method is to generate a synthetic CT (sCT) from the MR that can then be used to replace the conventional CT in the radiotherapy planning process. Three main approaches have been adopted for the prostate clinical site: bulk density assignments, regression-based methods and atlas-based methods, with the latter two being the most clinically appropriate (Johnstone et al. 2017). The attraction of atlas-based methods is that they do not require any specialist MR sequences, although they do require dedicated MR acquisition protocols which are optimised for geometric accuracy over the whole field of view (Paulson et al. 2015). Several groups have developed automatic or semi-automatic atlas-based methods of generating a sCT for prostate radiotherapy (Dowling et al. 2015, Siverson et al. 2015, Chen et al. 2016), which use an atlas of co-registered CT-MR pairs and deformable registration techniques to generate a sCT. Each of these algorithms use an atlas created from data acquired on the same MR scanner, at the same field strength. In addition both Dowling et al. and Chen et al. evaluated their methods using a ‘leave one out’ approach where one of the atlas pairs is used as the subject and remaining pairs used as the atlas.

For these algorithms to be applicable within a routine clinical setting it is important to evaluate them using data different to the atlas data. This is because the performance of an atlas-based algorithm depends on the registration quality between the incoming

image and the atlas (Despotović et al. 2015). The quality of the registration in turn depends on the similarity of the incoming MR image to the atlas images. MR images can vary substantially depending on the scanner, acquisition sequence and patient (Nyúl et al. 1999). There can still be significant variations between different scanners and vendors even when using the same sequence and acquisition parameters (Bauer et al. 2010). These image variations can influence the performance of segmentation algorithms (Udupa et al. 2006). Small differences in acquisition parameters can also change the contrast in the images (Fischl et al. 2004) and the accuracy of atlas-based segmentation algorithms often reduces when images with different contrasts to the atlas images are used (Han & Fischl 2007). In particular MR images acquired at a different field strength to the atlas images can have significantly different signal to noise and contrast to noise ratios (Soher et al. 2007) as well as increased magnetic susceptibility effects and image intensity non-uniformities (Chow et al. 2015). Jovicich et al. found that changing the field strength changed the results of an atlas-based segmentation algorithm for the brain (Jovicich et al. 2009). Similarly Chow et al. found some significant differences in atlas-based segmented volumes of the brain in the same subjects at 1.5 T and 3 T (Chow et al. 2015). Images acquired at different field strengths will also differ due to chemical shift and Gibb's (signal truncation) artefacts (Dietrich et al. 2008). All of these image variations mean data acquired on different scanners to those in the atlas could result in sub-optimal registrations to the atlas MR's and so adversely impact the quality of the synthetic CT produced. Therefore it is important to validate atlas-based sCT algorithms using different data to those in the atlas, and in particular acquired at a different field strength. This study aimed to investigate the generalisation of the Dowling algorithm by evaluating it using data acquired at a different field strength with a different MR scanner in a different centre.

2. Methods

2.1. Patient Data Collection

This was a retrospective study involving prostate radiotherapy patients at the Northern Centre for Cancer Care. Patients were selected from two time periods (01/12/2015 - 13/01/2016 and 12/05/2016 - 22/06/2016). The following exclusion criteria were applied (number of patients excluded): hip prostheses (2), post-prostatectomy (0), the patient external contour was larger than the maximum MR field of view (13) and gross patient motion artefact (1). Gross patient motion artefact was determined qualitatively and defined by significant blurring and ghosting in the phase encode direction. 21 patients were included in this study with an inclusion rate of 54%. Patients were aged between 54 and 79 years, with the median age being 70 years. All patients had been diagnosed with prostate cancer (stages T1 to T3). Each patient received a planning MR (1.5 T Magnetom Espree, Siemens, Erlangen, Germany) and CT (Sensation Open, Siemens, Erlangen, Germany) scan as part of the routine radiotherapy planning procedure. All

patient scans were anonymised prior to being included in the study.

Both CT and MR scans were performed on flat couch tops with the patients in the local standard prostate radiotherapy immobilisation. All patients underwent routine bladder and bowel preparation prior to each scan. The bladder preparation protocol consisted of an empty bladder 30 minutes prior to the scan, followed by drinking 400 ml of water. The bowel preparation protocol required application of a micro-enema 45 minutes prior to the scan followed by bowel emptying. Internal fiducial markers were not present in any patient. To avoid distorting the external patient contour the MR images were acquired using a 6 channel flexible receive coil (Siemens Body Matrix) supported over the patient by an in-house manufactured coil bridge and the 24 channel spine receive coil contained in the couch (Siemens Spine Matrix).

The MR images were acquired using the same pulse sequence and similar acquisition parameters as used in Dowling et al. (Dowling et al. 2015). The acquisition parameters in this study were not identical to those used in Dowling et al. as the data in this study was acquired as part of the routine planning MR scan and used retrospectively. The MR images in this study were acquired with a T2-weighted SPACE (Sampling Perfection with Application optimised Contrasts using different flip angle Evolution) sequence. This is a 3D turbo spin echo sequence with a repetition time $TR = 1500$ ms, an echo time $TE = 210$ ms and a constant flip angle $\alpha = 150^\circ$. The echo train length was 85 with an echo spacing of 3.82 ms. The Field of View (FoV) was 450×450 mm² for all patients, encompassing the entire patient external contour, with a voxel size $1.8 \times 1.8 \times 1.7$ mm³. 120 slices were acquired giving a longitudinal scan length of 204 mm for all patients. The receive bandwidth was large, $\Delta f = 592$ Hz \cdot [pixel]⁻¹ and the Siemens 3D distortion correction algorithm was applied to reduce the geometric distortion in the images. The main differences to the parameters used by Dowling et al. were the resolution of the 3 T atlas images (voxel size $1.6 \times 1.6 \times 1.6$ mm³) and the T1-weighting (repetition time $TR = 1200$ ms and flip angle $\alpha = 135^\circ$). The echo time of the atlas images ($TE = 97$ ms) was approximately half the echo time used in this study. The CT images were acquired in this study with a voxel size of $1.1 \times 1.1 \times 3$ mm and a tube voltage of $V = 120$ kVp. A representative planning CT and MR are shown in figure 1.

2.2. Synthetic CT Generation

The sCT's were generated using the Dowling algorithm as described previously (Dowling et al. 2015). The algorithm is briefly summarised here for convenience:

- (i) The atlas consisted of 39 CT-MR pairs acquired on a 3 T MR scanner (Skyra, Siemens) and one of two CT scanners (LightSpeedRT, GE Healthcare, Wisconsin, USA and Aquilion, Toshiba, Tokyo, Japan). Each MR image was preprocessed through bias field correction, histogram equalisation and smoothing via gradient anisotropic diffusion. Each atlas CT was registered to the atlas MR using a robust rigid registration followed by a structure guided deformable registration.

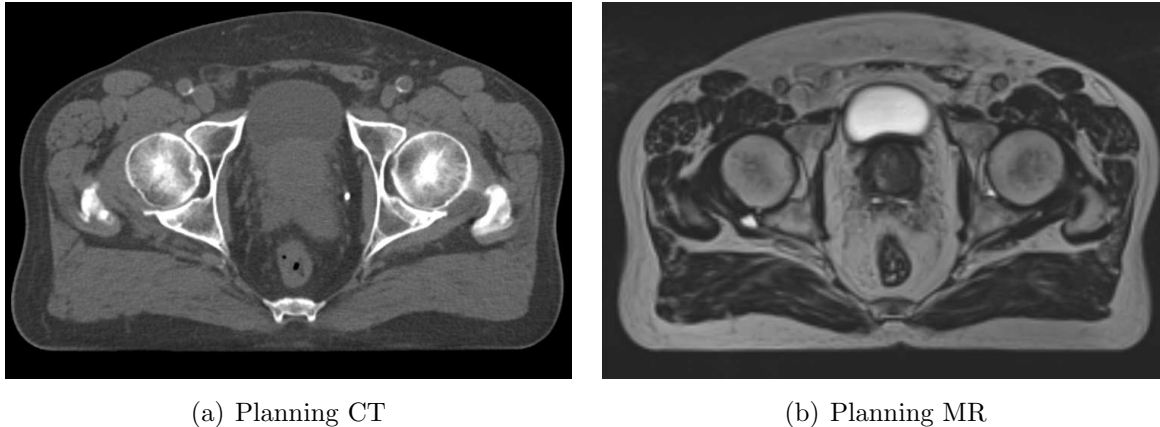


Figure 1: An example of the planning CT (a) and MR (b). The MR is taken in the treatment position on a flat top couch and with the receive coils supported above the patient surface.

- (ii) The incoming MR is preprocessed as described in step (i). Each atlas MR was registered to the incoming MR using the same robust rigid registration as above, followed by a deformable registration (not structure-guided).
- (iii) These deformation fields are applied to each corresponding atlas CT.
- (iv) The deformed atlas CT's are combined together to create a sCT using local voting. This compares a small patch (radius two voxels) around each voxel in the incoming MR with the equivalent patch in each of the registered atlas MR's. The normalised sum of squared differences is computed for each atlas MR, which are used to weight the contribution to each sCT voxel from the corresponding atlas CT.
- (v) The external body contour of the sCT is grown isotropically by one voxel using a nearest neighbour interpolation. This accounted for an observed systematic difference in body shape between the MR and CT. The contour expansion was assigned a uniform value of 47 HU, based on the average value of the outer 1 mm of the skin layer in planning CT images of the pelvis.

The parameters used within the local weighted voting component of the algorithm were a patch radius of 2 voxels and a gain of 1, matching those used in Dowling et al. In the Dowling algorithm the body contour expansion was added to account for an observed systematic difference in body contour between the 3 T T2-weighted MR images and the CT images. This was hypothesised to be due to MR signal loss in the outer skin layer (Dowling et al. 2015). It has not been established whether this expansion was required at 1.5 T. Therefore in this study two sets of sCT images were created, one with the one voxel body contour expansion as described in Dowling et al. (sCT_{1V}) and one without the contour expansion (sCT), omitting step 5. above (see figure 2).

2.3. Evaluation

The planning CT (pCT) was registered to both the sCT and sCT_{1V} using RayStation's (version 5, RaySearch Laboratories, Stockholm, Sweden) automatic intensity-based

Synthetic CT		Planning CT	
HU	Mass Density/g · cm ⁻³	HU	Mass Density/g · cm ⁻³
-1000	0.0001	-971	0.001
-791	0.2	-710.2	0.3
-506	0.5	-569.6	0.45
-26	0.99	-89.7	0.92
-1	1	-2.7	1.015
45.5	1.06	83.5	1.08
53.5	1.07	166	1.17
231	1.16	440.1	1.34
992	1.61	784.6	1.56
3403	2.87	1178.2	1.84

Table 1: The HU - mass density calibration curves used for the synthetic CT’s and planning CT.

mutual information rigid registration algorithm. The two registrations (pCT to sCT and pCT to sCT_{1V}) were carried out independently. This ensured each synthetic CT was optimally registered to the pCT, but resulted in the two registrations being slightly different. This difference was quantified by calculating the mean of the differences in each translation and rotation axis.

RayStation enables multiple Hounsfield Unit (HU) - mass density calibration curves to be used. Therefore two different curves were used in this study, one to calibrate each pCT and one to calibrate the synthetic CT’s. The two curves used are given in table 1. The pCT curve used was the clinical HU - mass density calibration curve for the local CT scanner. The synthetic CT’s are produced from a combination of the atlas CT’s. Therefore the appropriate HU calibration curve to use is the curve for the CT’s contained in the atlas. The Dowling algorithm includes atlas patients from two different CT scanners with two different HU - mass density calibration curves. Therefore a composite curve of the unweighted average of the two curves was used for the synthetic CT’s. This could introduce a small confounding dose error if a particular synthetic CT was heavily weighted towards atlas CT scans from only one of the CT scanners. To estimate this error a treatment plan was recalculated three times on one patient sCT: once with each of the atlas scanner calibration curves and once with mean curve that was used in the evaluation. The dose difference at isocentre with each calibration curve was calculated.

The external contour was automatically outlined on each dataset with a Hounsfield Unit threshold of $T = -250$ HU. The external contours of the sCT and sCT_{1V} were compared to the planning CT external contour using the Dice similarity coefficient (DSC), mean and maximum distance to agreement (DTA_{mean} and DTA_{max}), which were calculated using RayStation.

After the image registration was carried out the clinical structure set was copied

from the pCT onto both the sCT and sCT_{1V} using the relevant registration matrix. The structure set was based on the CHHiP trial with three Planning Target Volumes (PTV) (Dearnaley et al. 2016). The clinical structure set was not modified after transfer and was used to enable dose volume histogram points of the central PTV (PTV3) to be compared. The automatically generated contours produced by the Dowling algorithm were not evaluated in this study.

A 6 MV Volumetric Modulated Arc Therapy (VMAT) plan was created on the pCT. The local clinical plan protocol was used, consisting of a single 360° arc plan with a 5 degree collimator rotation and a prescription of 60 Gy in 20 fractions to 50% of PTV3. The local class solution was applied and the plan optimised until the difference in cost function between consecutive iterations fell below a set threshold or when 40 iterations was reached, whichever occurred first. A final dose calculation was then performed on the optimised plan with a 2 × 2 × 2 mm³ dose grid. The treatment plan was recalculated on both the sCT and sCT_{1V} keeping the monitor units and the dose grid voxel size and position the same. The percentage difference in isocentre dose between each synthetic CT and the pCT was calculated using

$$\Delta D_{sCT}^{HU} = 100 \frac{D_{sCT} - D_{pCT}}{D_{pCT}}, \quad (1)$$

where D_{sCT} was the dose at the isocentre for the sCT, D_{pCT} was the dose at the isocentre for the pCT and HU indicates that a Hounsfields Units (HU) based density correction was used in the dose calculation. An equivalent equation was used for the dose difference between sCT_{1V} and the pCT, $\Delta D_{sCT_{1V}}^{HU}$. The percentage doses differences for the PTV3 Dose Volume Histogram (DVH) points D98, D95, D50, D5 and D2 were also calculated for both sCT and sCT_{1V} using the same method.

A gamma analysis was performed comparing the dose calculated on the pCT to the dose calculated on the sCT and sCT_{1V}. The gamma analysis was calculated using the SlicerRT toolkit within the open-source 3D Slicer application (version 4.6.2, www.slicer.org) (Fedorov et al. 2012, Pinter et al. 2012). A 3D global gamma analysis was carried out with the following criteria: dose difference 1% of prescription dose (60 Gy) and distance to agreement 1 mm, dose difference 1% and distance to agreement 2 mm and dose difference 2% and distance to agreement 2 mm. The gamma analysis was carried out within the external contour only and with all dose points below a threshold of 10% of the prescription dose (60 Gy) excluded.

In order to determine the effect of inter-scan body contour differences between pCT and synthetic CT's due to the scans being acquired in separate imaging sessions, the density for each image dataset was over-ridden and set to unity, $\rho = 1 \text{ g} \cdot \text{cm}^{-3}$ (i.e. water). The treatment plan was recalculated on all three image datasets, keeping the monitor units and the dose grid constant. Therefore the only difference between the synthetic CT's and the pCT was the external contour. The percentage dose differences in isocentre dose and the five PTV3 DVH points defined earlier were calculated.

Finally the radiological water equivalent isocentre depth for the VMAT plan was calculated at 4° angles for each image in the plane of the isocentre, following Siverson

Image	Density	% Dose Difference				
		D98	D95	D50	D5	D2
sCT	HU	1.0 (3.2)	1.0 (3.1)	1.0 (2.9)	1.1 (3.2)	1.1 (3.4)
sCT	Water	1.2 (2.4)	1.2 (2.4)	1.1 (2.2)	1.1 (2.3)	1.1 (2.4)
sCT _{1V}	HU	-0.7 (-2.2)	-0.7 (-2.2)	-0.7 (-1.7)	-0.7 (-1.4)	-0.7 (-1.6)
sCT _{1V}	Water	-0.5 (-1.3)	-0.6 (-1.3)	-0.6 (-1.3)	-0.6 (-1.4)	-0.6 (-1.3)

Table 2: The mean (maximum) percentage dose differences (synthetic CT minus planning CT as a percentage of the planning CT) at different PTV3 DVH points for both synthetic CT’s for all patients (n=21). The density indicates the density correction used within the dose calculation (HU = Hounsfield Units, Water = $1 \text{ g} \cdot \text{cm}^{-3}$).

et al. (Siversson et al. 2015). This radiological equivalent depth was calculated by RayStation using the HU value of each voxel and the relevant HU - electron density curve (table 1). The physical isocentre depth for each angle was also calculated. The mean difference in equivalent and physical isocentre depth between each synthetic CT and the pCT for each patient was calculated.

3. Results

The percentage dose difference at the isocentre between the pCT and the sCT and sCT_{1V} respectively was $\Delta D_{sCT}^{HU} = 0.9 \pm 0.8$ (-0.5, 2.9) % and $\Delta D_{sCT_{1V}}^{HU} = -0.7 \pm 0.7$ (-2.1, 0.9) %, results given as mean \pm one standard deviation (minimum, maximum). The equivalent results using the water density correction in the calculation were within 0.2 %, $\Delta D_{sCT}^W = 1.1 \pm 0.5$ (0.1, 2.3) % and $\Delta D_{sCT_{1V}}^W = -0.6 \pm 0.5$ (-1.2, 0.4) %. The percentage differences at a range of PTV3 DVH points are given in table 2. An example dose distribution on the planning CT and both synthetic CT’s for a typical patient is shown in figure 2. The dose difference maps for the sCT and sCT_{1V} for the same patient are shown in figure 3.

The maximum error arising from using a composite HU-mass density calibration for the synthetic CT’s was a 0.1 % dose difference at the isocentre. This was true for both the sCT and sCT_{1V}.

The results of the comparison between the external contours on the pCT and synthetic CT’s are shown in table 3. The mean results for the sCT_{1V} were closer to the pCT external contour than the sCT for each metric. However the differences were small and agreed within one standard deviation.

The differences between the two registrations (pCT to sCT and pCT to sCT_{1V}) were small. The mean translation difference in the inferior-superior direction (the largest) was $\Delta t = 0.17 \pm 0.18$ cm (\pm one standard deviation) and the mean rotational difference in the pitch direction (the largest) was $\Delta r = 0.13 \pm 0.55^\circ$.

The mean difference in equivalent isocentre depth for the sCT was $\Delta z_{sCT}^{equiv} = -2.1 \pm 1.9$ (-6.2, 2.7) mm and for the sCT_{1V} $\Delta z_{sCT_{1V}}^{equiv} = 1.6 \pm 1.9$ (-2.4, 6.4) mm,

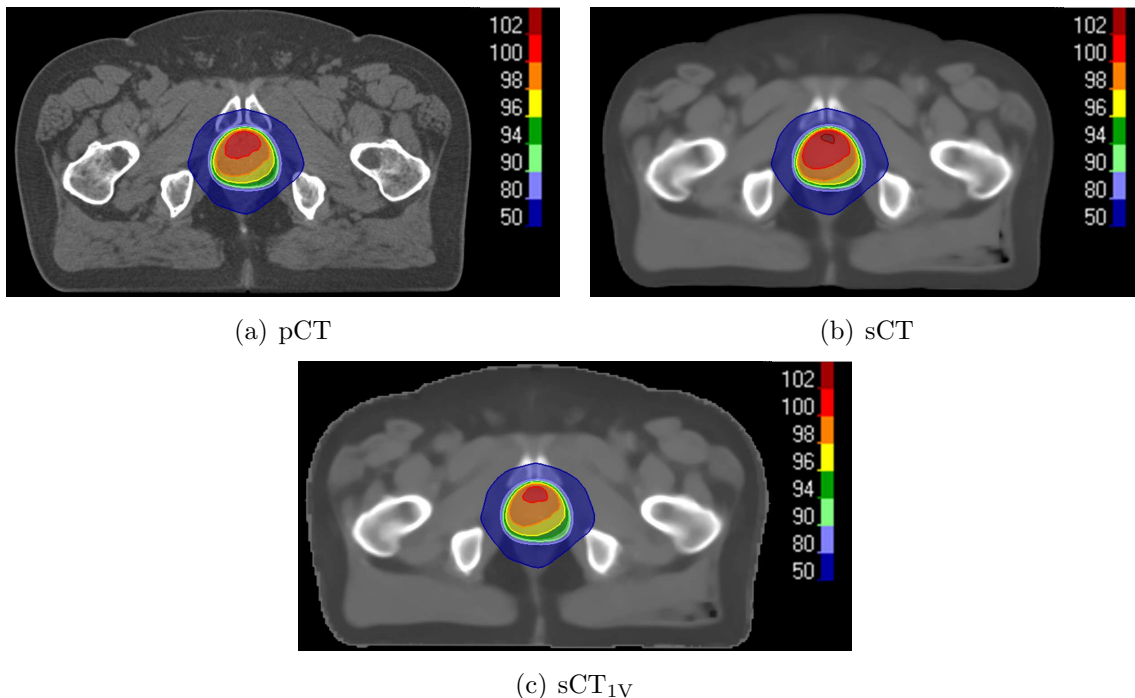


Figure 2: An example dose distribution on the pCT (a), sCT (b) and sCT_{1V} (c). Isodoses are shown as percentages of the prescription dose (60 Gy). The isocentre dose differences for this patient were $\Delta D_{sCT}^{HU} = 1.2\%$ and $\Delta D_{sCT_{1V}}^{HU} = -0.4\%$. The gamma pass rates were $\Gamma_{sCT} = 93.9\%$ and $\Gamma_{sCT_{1V}} = 99.4\%$.

Metric	sCT	sCT _{1V}
DSC	0.94 ± 0.02 (0.87, 0.97)	0.95 ± 0.03 (0.88, 0.98)
DTA _{mean} /cm	0.45 ± 0.19 (0.26, 1.16)	0.42 ± 0.22 (0.22, 1.10)
DTA _{max} /cm	2.62 ± 0.80 (1.58, 4.50)	2.25 ± 0.81 (1.21, 4.40)

Table 3: The mean \pm standard deviation (minimum, maximum) result for each comparison metric comparing the external contour of the synthetic CT to the pCT. DSC is the dice similarity coefficient, DTA_{mean} is the mean distance to agreement and DTA_{max} the maximum distance to agreement. DSC is a dimensionless comparison metric and the two distance to agreement metrics are given in cm.

results given as mean \pm one standard deviation (minimum, maximum). The mean difference in physical isocentre depth was $\Delta z_{sCT}^{phys} = -2.6 \pm 1.1$ (-4.9, -1.0) mm and $\Delta z_{sCT_{1V}}^{phys} = 1.2 \pm 1.1$ (-1.2, 2.7) mm for the sCT and sCT_{1V} respectively.

The gamma analysis pass rates are given in table 4. Figure 4 gives example gamma maps for the same patient shown in figure 2.

4. Discussion

The aim of this study was to evaluate an atlas-based synthetic CT algorithm using MR data acquired at a different field strength and centre. The algorithm was evaluated with

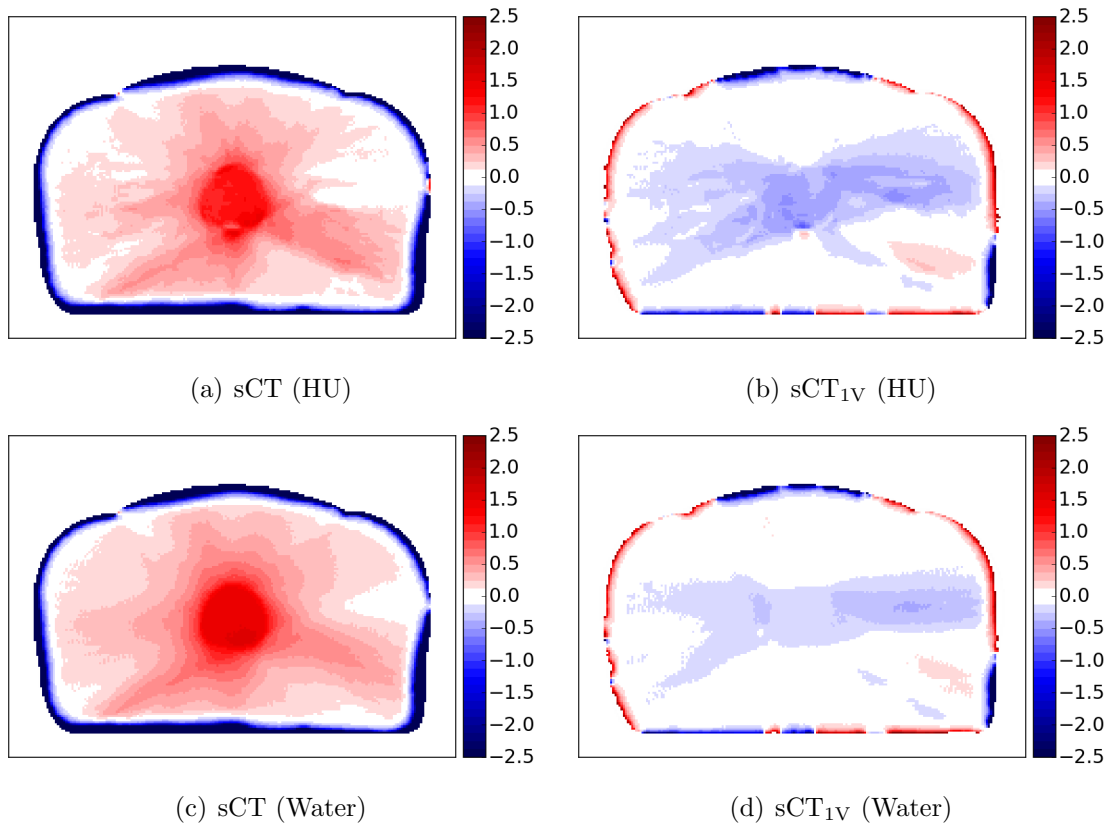


Figure 3: The dose difference maps for the sCT (a) and sCT_{1V} (b) calculated using the HU density correction for the same patient shown in figure 2. The equivalent dose difference maps calculated with the density set to unity for the pCT and the sCT (c) and sCT_{1V} (d). Dose differences are shown as a percentage of the prescription dose (60 Gy).

Image	Gamma Pass Rate/%		
	1%/1 mm	1%/2 mm	2%/2 mm
sCT	91.1 ± 7.0 (72.2, 97.1)	92.6 ± 6.0 (76.6, 97.7)	96.1 ± 2.9 (88.2, 98.6)
sCT _{1V}	95.2 ± 2.9 (88.3, 98.5)	96.0 ± 2.3 (90.7, 98.7)	98.8 ± 0.5 (97.6, 99.5)

Table 4: The mean ± standard deviation (minimum, maximum) gamma pass rates for the sCT and sCT_{1V} over the whole study population. The pass rates are shown for the three different gamma criteria.

and without a one voxel body contour expansion to determine if this was necessary at 1.5 T.

Our results appear to show that the one voxel body contour expansion is required at 1.5 T. This can be seen dosimetrically with the mean isocentre dose differences from the pCT and all the PTV3 DVH points being smaller, and the gamma pass rates higher, for the sCT_{1V} compared to the sCT. In addition, geometrically the differences in equivalent and physical isocentre depth with the sCT_{1V} were closer to zero than for the sCT. The change in physical isocentre depth difference for the sCT and sCT_{1V} was

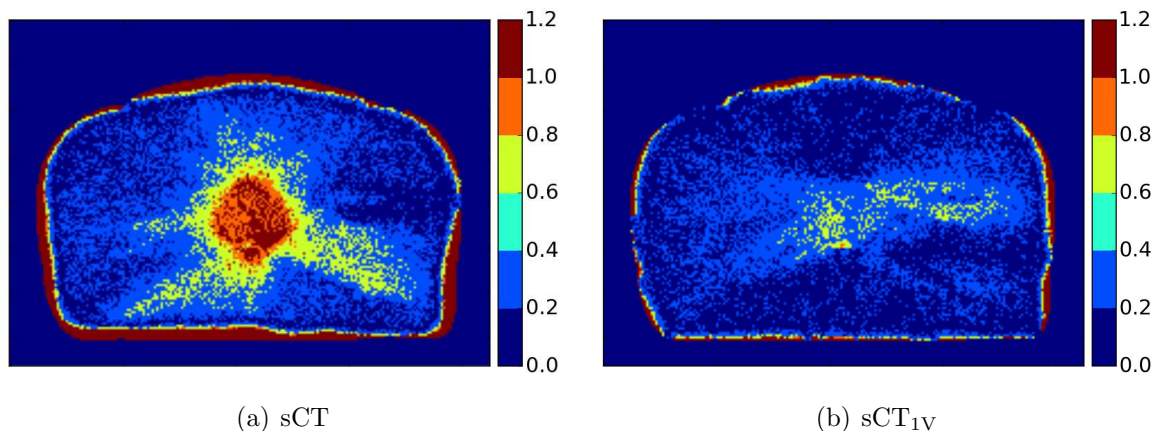


Figure 4: Example gamma map for the sCT (left) and sCT_{1V} (right) for the same patient shown in figure 2. Gamma criteria were 1% global dose difference and 1 mm distance to agreement.

3.8 mm, significantly larger than 1.8 mm voxel expansion expected. This is primarily due to the nearest neighbour interpolation method used to produce the body contour expansion, which results in larger than one voxel expansions in areas where the body contour is curved. This 3.8 mm mean difference in isocentre depth is consistent with the observed dose difference at isocentre between sCT and sCT_{1V} of 1.7%. Finally the sCT_{1V} external contour agreed better with pCT external contour on the comparison metrics investigated, although the differences were small and insignificant. There is an apparent discrepancy between the mean distance to agreement metric and the physical isocentre depth difference. This is likely to be due to the distance to agreement metric including the differences between the pCT and synthetic CT's in the superior and inferior directions, as well as axially.

The sCT_{1V} seems to over-correct the systematic difference in body contour expansion, with only two patients (10%) having a negative physical isocentre depth difference. This may be due to the MR images in this study having a larger voxel size than used in Dowling et al, which would produce a larger expansion. This indicates a limitation to the generalisation of this algorithm since it will depend on the voxel size of the MR images, with the algorithm requiring the voxel size to be 'similar' to that found in the atlas. Further work would be required to investigate how sensitive the algorithm is to differences in MR voxel size.

There will be small differences in body contour shape between the pCT and planning MR (and therefore the synthetic CT's) because the scans were acquired in separate imaging sessions (Maspero et al. 2017). These inter-scan differences will introduce a confounding error into the dosimetric evaluation by generating dosimetric differences that are not due to errors in the Hounsfield Units within the synthetic CT's but in the differences in body contour shape to the pCT. The dose differences calculated with the densities of the synthetic CT's and the pCT over-ridden to water indicate the magnitude of the dose differences caused by these inter-scan differences. The water calculated

isocentre dose differences were within 0.2 % to those measured with Hounsfield Units and appeared very similar (see figure 3). This suggests that a significant contribution to the observed dose differences are due to inter-scan differences in body contour, rather than errors in Hounsfield Unit assignment.

The mean isocentre dose difference to the sCT_{1V} in this study agreed within one standard deviation of the result reported by Dowling et al., $\Delta D = -0.3 \pm 0.8$ (−1.5, 1.8) % (Dowling et al. 2015). Similarly the sCT_{1V} mean dose differences for the DVH points evaluated all agreed within one standard deviation and the median gamma pass rates agreed within 3% with those presented in Dowling et al. This suggests that the Dowling algorithm with body contour expansion is generalisable to 1.5 T data acquired at a different centre with a similar MR voxel size.

This is an important result because it demonstrates that the preprocessing steps contained in the algorithm are able to mitigate the image intensity differences between MR images acquired on different scanners sufficiently to not degrade the image registration quality (Despotović et al. 2015). This result also suggests that the algorithm is robust to the differences in contrast between images acquired with the same sequence and similar, but not identical, acquisition parameters (Han & Fischl 2007). In particular this study demonstrates that the algorithm can be used for images acquired at a different field strength to the atlas. This is in contrast to the results found for automatically segmented brain volumes using an atlas-based segmentation algorithm on 1.5 T and 3 T images (Jovicich et al. 2009, Chow et al. 2015). This may be because the effect of interest in this case, the calculated dose distribution, is less sensitive to small changes in synthetic CT and so the algorithm overall is less sensitive to changes in field strength. Susceptibility effects and chemical shift artefacts will be different at 1.5 T and 3 T, but were minimised in both sets of images by having large acquisition bandwidths (Soher et al. 2007). The chemical shift was ~ 0.6 pixels for the 3 T images and ~ 0.4 pixels for the 1.5 T images and therefore likely to have had a negligible impact on the image registration within the Dowling algorithm. Changing the field strength will also result in differences in Gibbs artefacts (Dietrich et al. 2008). However both sets of images had similar voxel sizes and good signal to noise ratios and so differences in Gibbs artefacts were also likely to minimally impact the registration quality. This may be another reason why the algorithm may not generalise very well for MR images acquired with significantly different voxel sizes.

This study has demonstrated that this algorithm will generalise to data acquired using a different scanner at a different field strength with the same sequence and similar acquisition parameters, notably a sufficiently high bandwidth and similar voxel size. These features are recommended for MR images acquired for radiotherapy planning to reduce geometric distortion and provide sufficient resolution for accurate contouring (Liney & Moerland 2014). Further work on evaluating the generalisation of this algorithm could include investigating data acquired with different vendor scanners and with larger differences in acquisition parameters.

The results from this study are similar to those reported in the literature for

other atlas-based methods of synthetic CT generation for the prostate. Siversson et al. reported a mean dose difference in the PTV D50 of $\Delta D_{50} = 0.1 \pm 0.4\%$ (mean \pm one standard deviation) when evaluated using data acquired at the same scanner as the atlas data and $\Delta D_{50} = 0.6 \pm 0.5\%$ using data acquired at a different scanner (Siversson et al. 2015). The authors did not specify how the dose difference was calculated so only the magnitude and not the sign of the dose difference can be compared to the results in this study. Chen et al. reported PTV D95 differences of $\Delta D_{95} = 0.1 \pm 0.1\%$ (mean \pm one standard deviation) (Chen et al. 2016). However the dose differences were evaluated after the sCT was deformably registered to the evaluation planning CT, thus ensuring the outer body contours were identical. This would remove a significant source of differences between the sCT and pCT, and therefore reduce the observed dose difference.

The results of this study compare favourably with other methods of sCT generation for the prostate. Lambert et al. used a bulk density method and found a isocentre dose difference of $\Delta D_{iso} = -1.3 \pm 0.8\%$ (mean \pm one standard deviation) (Lambert et al. 2011). Korhonen et al. used a dual model regression based technique and reported PTV D50 dose difference of $\Delta D_{50} = 0.3 \pm 0.2\%$ (mean \pm one standard deviation) (Korhonen et al. 2014). Kim et al. also used a regression based technique and found a mean PTV D95 dose difference of $\Delta D_{95} = 0.3\%$. A significant advantage of the atlas-based algorithm evaluated here is that it was automatic, which eliminates time consuming manual contouring.

5. Conclusion

This study has demonstrated that a 3 T atlas-based synthetic CT algorithm can be used on 1.5 T data acquired at a different centre using a similar MR acquisition protocol. The mean dose differences to the planning target volume were less than 1% and within one standard deviation of 0% difference. The one voxel body contour expansion contained in the Dowling algorithm improves the accuracy of the result compared to synthetic CT's without the expansion. This expansion step requires MR voxel sizes which are similar to those contained in the Dowling atlas, which limits the generalisation of the algorithm. Further work is needed to determine how close the voxel size needs to be in order to give accurate results. The algorithm only requires widely available, routine MR sequences and the entire process of synthetic CT generation is automatic. Further work is required to investigate the accuracy of synthetic CT's in on-treatment image verification using Cone Beam CT. The Dowling algorithm appears a good candidate for use within a clinical MR-only planning prostate radiotherapy workflow.

Acknowledgements

We gratefully acknowledge funding for this work received from The Sir John Fisher Foundation, the Leeds Institute of Cancer and Pathology (LICAP), the Institute of

Physics and Engineering in Medicine (IPEM) and Charlie Bear for Cancer Care, Newcastle upon Tyne Hospitals NHS Foundation Trust.

References

- Bauer C M, Jara H, Killiany R, Initiative A D N et al. 2010 Whole brain quantitative T2 MRI across multiple scanners with dual echo FSE: applications to AD, MCI, and normal aging *Neuroimage* **52**(2), 508–514.
- Chen S, Quan H, Qin A, Yee S & Yan D 2016 MR image-based synthetic CT for IMRT prostate treatment planning and CBCT image-guided localization *Journal of Applied Clinical Medical Physics* **17**(3).
- Chow N, Hwang K, Hurtz S, Green A, Somme J, Thompson P, Elashoff D, Jack C, Weiner M & Apostolova L 2015 Comparing 3T and 1.5 T MRI for mapping hippocampal atrophy in the Alzheimer’s Disease Neuroimaging Initiative *American Journal of Neuroradiology* **36**(4), 653–660.
- Dearnaley D, Syndikus I, Mossop H, Khoo V, Birtle A, Bloomfield D, Graham J, Kirkbride P, Logue J, Malik Z et al. 2016 Conventional versus hypofractionated high-dose intensity-modulated radiotherapy for prostate cancer: 5-year outcomes of the randomised, non-inferiority, phase 3 CHHiP trial *The Lancet Oncology* **17**(8), 1047–1060.
- Despotović I, Goossens B & Philips W 2015 MRI segmentation of the human brain: challenges, methods, and applications *Computational and mathematical methods in medicine* **2015**.
- Dietrich O, Reiser M F & Schoenberg S O 2008 Artifacts in 3-T MRI: physical background and reduction strategies *European journal of radiology* **65**(1), 29–35.
- Dowling J A, Sun J, Pichler P, Rivest-Hénault D, Ghose S, Richardson H, Wratten C, Martin J, Arm J, Best L et al. 2015 Automatic substitute computed tomography generation and contouring for magnetic resonance imaging (MRI)-alone external beam radiation therapy from standard MRI sequences *International Journal of Radiation Oncology* Biology* Physics* **93**(5), 1144–1153.
- Dubois D F, Prestidge B R, Hotchkiss L A, Prete J J & Bice Jr W S 1998 Intraobserver and interobserver variability of MR imaging-and CT-derived prostate volumes after transperineal interstitial permanent prostate brachytherapy. *Radiology* **207**(3), 785–789.
- Fedorov A, Beichel R, Kalpathy-Cramer J, Finet J, Fillion-Robin J C, Pujol S, Bauer C, Jennings D, Fennessy F, Sonka M et al. 2012 3d slicer as an image computing platform for the quantitative imaging network *Magnetic resonance imaging* **30**(9), 1323–1341.
- Fischl B, Salat D H, van der Kouwe A J, Makris N, Ségonne F, Quinn B T & Dale A M 2004 Sequence-independent segmentation of magnetic resonance images *Neuroimage* **23**, S69–S84.
- Han X & Fischl B 2007 Atlas renormalization for improved brain MR image segmentation across scanner platforms *IEEE transactions on medical imaging* **26**(4), 479–486.
- Johnstone E, Wyatt J J, Henry A M, Short S C, Sebag-Montefiore D, Murray L, Kelly C G, McCallum H M & Speight R 2017 A systematic review of synthetic CT generation methodologies for use in MRI-only radiotherapy *International Journal of Radiation Oncology* Biology* Physics* .
- Jovicich J, Czaner S, Han X, Salat D, van der Kouwe A, Quinn B, Pacheco J, Albert M, Killiany R, Blacker D et al. 2009 MRI-derived measurements of human subcortical, ventricular and intracranial brain volumes: reliability effects of scan sessions, acquisition sequences, data analyses, scanner upgrade, scanner vendors and field strengths *Neuroimage* **46**(1), 177–192.
- Khoo V & Joon D 2006 New developments in MRI for target volume delineation in radiotherapy *The British journal of radiology* .
- Korhonen J, Kapanen M, Keyriläinen J, Seppälä T & Tenhunen M 2014 A dual model hu conversion from MRI intensity values within and outside of bone segment for MRI-based radiotherapy treatment planning of prostate cancer *Medical physics* **41**(1), 011704.
- Lambert J, Greer P B, Menk F, Patterson J, Parker J, Dahl K, Gupta S, Capp A, Wratten C, Tang C

- et al. 2011 MRI-guided prostate radiation therapy planning: Investigation of dosimetric accuracy of MRI-based dose planning *Radiotherapy and Oncology* **98**(3), 330–334.
- Liney G P & Moerland M A 2014 Magnetic resonance imaging acquisition techniques for radiotherapy planning in ‘Seminars in radiation oncology’ Vol. 24 Elsevier pp. 160–168.
- Maspero M, Seevinck P, Schubert G, Hoesl M, van Asselen B, Viergever M, Lagendijk J, Meijer G & van den Berg C 2017 Quantification of confounding factors in mri-based dose calculations as applied to prostate imrt *Physics in Medicine and Biology* **62**(3).
- Nyholm T, Nyberg M, Karlsson M G & Karlsson M 2009 Systematisation of spatial uncertainties for comparison between a MR and a CT-based radiotherapy workflow for prostate treatments *Radiation Oncology* **4**(1), 1.
- Nyúl L G, Udupa J K et al. 1999 On standardizing the MR image intensity scale *image* **1081**.
- Paulson E S, Erickson B, Schultz C & Li X A 2015 Comprehensive MRI simulation methodology using a dedicated mri scanner in radiation oncology for external beam radiation treatment planning *Medical physics* **42**(1), 28–39.
- Pinter C, Lasso A, Wang A, Jaffray D & Fichtinger G 2012 Slicerrt: Radiation therapy research toolkit for 3D slicer *Medical physics* **39**(10), 6332–6338.
- Rasch C, Barillot I, Remeijer P, Touw A, van Herk M & Lebesque J V 1999 Definition of the prostate in CT and MRI: a multi-observer study *International Journal of Radiation Oncology* Biology* Physics* **43**(1), 57–66.
- Siversson C, Nordström F, Nilsson T, Nyholm T, Jonsson J, Gunnlaugsson A & Olsson L E 2015 Technical note: MRI only prostate radiotherapy planning using the statistical decomposition algorithm *Medical physics* **42**(10), 6090–6097.
- Soher B J, Dale B M & Merkle E M 2007 A review of MR physics: 3T versus 1.5 T *Magnetic resonance imaging clinics of North America* **15**(3), 277–290.
- Udupa J K, LeBlanc V R, Zhuge Y, Imielinska C, Schmidt H, Currie L M, Hirsch B E & Woodburn J 2006 A framework for evaluating image segmentation algorithms *Computerized Medical Imaging and Graphics* **30**(2), 75–87.